Atomistic modeling of electron-phonon interaction and electron mobility in Si nanowires

Yamada, Yoshihiro
Tsuchiya, Hideaki
Ogawa, Matsuto

(Citation)
Journal of Applied Physics,111(6):063720-063720

(Issue Date)
2012-03-15

(Resource Type)
journal article

(Version)
Version of Record

(URL)
https://hdl.handle.net/20.500.14094/90001668

Atomistic modeling of electron-phonon interaction and electron mobility in Si nanowires

Y. Yamada,[1,a)] H. Tsuchiya,[1,2] and M. Ogawa[1]
[1]*Department of Electrical and Electronic Engineering, Graduate School of Engineering, Kobe University, Kobe 657-8501, Japan*
[2]*Japan Science and Technology Agency, CREST, Chiyoda, Tokyo, 102-0075, Japan*

(Received 21 October 2011; accepted 22 February 2012; published online 29 March 2012)

We investigate the electron mobility of Si nanowires with ⟨100⟩, ⟨110⟩, and ⟨111⟩ crystalline orientations by considering atomistic electron-phonon interactions. We calculate the electron band structures based on a semiempirical $sp^3d^5s^*$ tight-binding approach and the phonon band structures based on the Keating potential model. Then, by combining the electron and phonon eigenstates based on Fermi's golden rule and solving the linearized Boltzmann transport equation while considering Pauli's exclusion principle, we evaluate the electron mobility of Si nanowires. As expected, phonons in Si nanowires are found to behave quite differently from phonons in bulk Si because of phonon confinement. However, electron mobility in Si nanowires is primarily governed by the variation in the electron effective mass rather than that of the phonon eigenstates. As a result, the ⟨110⟩-oriented Si nanowires showed the highest electron mobility, because they have the smallest electron effective mass among the three orientations. © *2012 American Institute of Physics*. [http://dx.doi.org/10.1063/1.3695999]

I. INTRODUCTION

The continuing downscaling of metal-oxide-semiconductor field-effect transistors (MOSFETs) has required the introduction of innovative device architectures in integrated logic circuit technology. In particular, to suppress short channel effects, the device structure is expected to change from a conventional planar structure with a single-gate electrode to a nonplanar structure with multi-gate electrodes. Si nanowire MOSFETs with the gate-all-around (GAA) configuration, which provides superior gate electrostatic control over the channel, are thus one of the most promising candidates for future high-performance integrated circuit devices. Practical fabrication of Si nanowire MOSFETs with diameters of less than 5 nm has already been reported.[1]

As the diameter of Si nanowires shrinks down to the nanometer scale, the number of atoms in the cross-section becomes countable, and hence the crystalline orientation, quantum confinement, and electron scattering play important roles in understanding the physical and transport characteristics of Si nanowires. Also, for exploration of novel functional materials and devices in the nanometer regime, a fully atomistic simulation considering both the electron and phonon band structures and their interactions is strongly required.

In conventional and commonly-used theoretical approaches, the transport properties of Si nanowires, such as carrier mobility, have been calculated by using an analytical effective mass band structure for electrons and bulk dispersion relations for phonons, where two-dimensional Schrödinger-Poisson equations are solved self-consistently.[2–5] Also, in modeling of phonon scattering processes, deformation potentials for the acoustic and optical phonons are parameterized to reproduce the experimental data for various semiconductor materials,[6] and thus atomistic details, such as crystalline orientation and cross-sectional shape are disregarded. However, because the lattice vibration in nanowires is quite different to that in bulk materials because of the phonon confinement, as demonstrated in this paper, the deformation potentials in nanowires may depend on both the diameter and the crystal orientation.[7,8] Generally speaking, the deformation potentials depend not only on the electron wave functions at the initial and final states, but also on the relevant phonon polarization vectors.[10] Therefore, atomistic treatment of the electron-phonon interaction is essential to predict the ultimate device performance of Si nanowire MOSFETs.

In this paper, we address this subject and investigate the electron mobility of Si nanowires with three crystalline orientations, ⟨100⟩, ⟨110⟩, and ⟨111⟩, by considering the atomistic electron-phonon interactions. We calculate the electron band structures based on a semiempirical $sp^3d^5s^*$ tight-binding (TB) approach,[11,12] and the phonon band structures based on the Keating potential model.[13] Then, by combining the electron and phonon eigenstates in Si nanowires, we derive the phonon scattering rate based on Fermi's golden rule. We then solve the Boltzmann transport equation while considering Pauli's exclusion principle and eventually evaluate the electron mobility of Si nanowires. We show that the electron mobility of Si nanowires strongly depends on the crystalline orientation and diameter, and its origin is discussed in terms of electron and phonon band structure modulation caused by the quantum confinement.

II. BAND STRUCTURE CALCULATIONS

Figure 1 shows unit cells of Si nanowires with cylindrically-shaped cross-sections, where we considered the three crystalline orientations of (a) ⟨100⟩, (b) ⟨110⟩, and (c) ⟨111⟩. The nanowire length is assumed to be infinite in the transport direction z, which is perpendicular to the plane

[a)]Author to whom correspondence should be addressed. Phone/Fax: +81-78-803-6082. Electronic mail: 065t804t@stu.kobe-u.ac.jp.

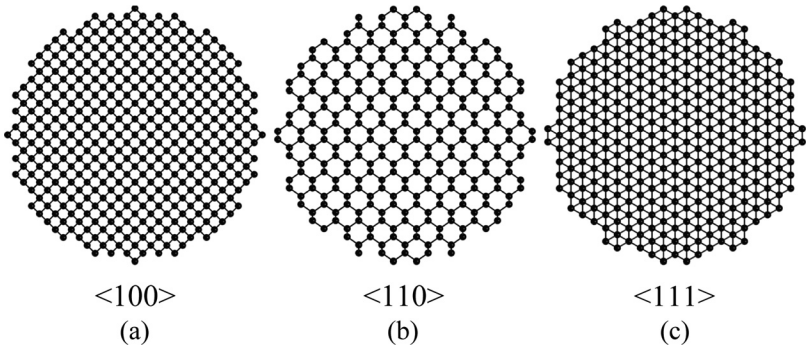

FIG. 1. Atomic models for (a) ⟨100⟩-oriented, (b) ⟨110⟩-oriented, and (c) ⟨111⟩-oriented Si nanowires with cylindrically-shaped cross-sections. The diameter is approximately 4.3 nm.

of the paper. The Si atoms are represented by spheres, and the surface Si atoms are passivated using an sp^3 hybridization scheme,[14] although their terminating hydrogen atoms are not shown in Fig. 1. The diameter of the Si nanowires is determined by the formula $D = 2\sqrt{a^3 N_{Si}/8\pi L}$, where a is the Si lattice constant of 5.43 Å, N_{Si} is the number of Si atoms, and L is the length of the unit cell along the transport directions, which corresponds to $L = a$, $a/\sqrt{2}$, and $\sqrt{3}a$ for the ⟨100⟩, ⟨110⟩, and ⟨111⟩ orientations, respectively.

A. Electrons

The electron band structures in Si nanowires were computed using a semiempirical TB approach, where the first nearest-neighbor and two-center orthogonal $sp^3d^5s^*$ model was used. Here, we give an outline of the computational procedure. First, the electronic wavefunction $\psi^n_{\kappa,\gamma}(k)$ is expressed in the form of a linear combination of atomic orbitals using Bloch-symmetrized atomic orbitals $\chi^n_{\kappa,\gamma}(k)$ as follows:

$$\psi^n(\mathbf{r},k) = \sum_{\kappa}\sum_{\gamma} c^n_{\kappa,\gamma}(k)\chi^n_{\kappa,\gamma}(\mathbf{r},k), \tag{1}$$

where n is the band index, $\mathbf{r}$ is the position vector, k is the wavenumber, κ is the atomic index, and γ represents the $sp^3d^5s^*$ TB orbitals. Because $\chi^n_{\kappa,\gamma}(\mathbf{r},k)$ can be expressed as a Fourier transform of the atomic orbitals $\varphi_{\kappa,\gamma}(\mathbf{r}-\mathbf{R}_{\eta\kappa})$, which are localized at the position (specified as $\mathbf{R}_{\eta\kappa}$) of the κ th Si atom in the η th unit cell as shown in Fig. 2, we obtain the following equation for $\chi^n_{\kappa,\gamma}(\mathbf{r},k)$:

$$\chi^n_{\kappa,\gamma}(\mathbf{r},k) = \frac{1}{\sqrt{N}}\sum_{\eta=1}^{N} e^{ik\eta L}\varphi_{\kappa,\gamma}(\mathbf{r}-\mathbf{R}_{\eta\kappa}), \tag{2}$$

where N is the number of unit cells. By substituting Eqs. (1) and (2) into the Schrödinger equation, we obtain an eigenvalue equation represented by the $sp^3d^5s^*$ TB orbital basis set as follows:

$$\sum_{(\eta',\kappa')\in NN(\eta,\kappa)}\sum_{\gamma'} U^{\gamma,\gamma'}_{\eta\kappa,\eta'\kappa'} e^{ik(\eta'-\eta)L} c^n_{\kappa',\gamma'}(k) - \phi_\kappa c^n_{\kappa,\gamma}(k) = E_n(k)c^n_{\kappa,\gamma}(k), \tag{3}$$

where spin-orbit interactions are not considered. The interatomic potential $U^{\gamma,\gamma'}_{\eta\kappa,\eta'\kappa'}$ in Eq. (3) can be formulated in terms of two-center integrals and directional cosines.[11] In this study, we used Boykin's parameterization[15] for the onsite energies and the two-center integrals between the nearest-neighbor Si atoms. ϕ_κ is the electrostatic potential obtained from the three-dimensional Poisson equation, which is solved by using the finite volume discretization scheme described in Appendix A until a self-consistently converged solution for ϕ_κ is obtained. Because the main purpose of this paper is to evaluate electron mobility under a low electric field, the Fermi level of the surrounding metallic gate was fixed to the conduction band minima of bulk Si, which means a zero flat-band voltage, and the gate voltage was set to zero for all simulations. Therefore, the self-consistent solution for the electrostatic potential coupled with the Poisson equation plays only a minor role in the present mobility estimation. We confirmed this by performing a non-self-consistent calculation in solving Eq. (3), and found that the self-consistent electrostatic potential has a negligibly small impact on determination of the electron mobility. However, the gate bias dependence of the electron mobility will be important for discussion of the on-state properties of Si nanowire MOSFETs, and our self-consistent approach is applicable to such simulations.

By diagonalizing the TB matrix at a given wavenumber k, the energy levels $E_n(k)$ and the expansion coefficients $c^n_{\kappa,\gamma}(k)$ are obtained for the electrons. As for the numerical values, the TB Hamiltonian of Eq. (3) is a sparse matrix with a dimension of 10 N_{Si} for the $sp^3d^5s^*$ ten orbital basis and N_{Si} atoms, and we therefore adopted the Jacobi-Davidson method[17] to solve Eq. (3) because a few eigenvalue spectra above the conduction band minima are usually relevant to the present carrier transport. Acceleration of the numerical convergence in the Jacobi-Davidson iterations was achieved by using the preconditioned generalized minimum residual solver (GMRES),[18] where a preconditioner was factorized using the incomplete Cholesky decomposition,[18] and matrix

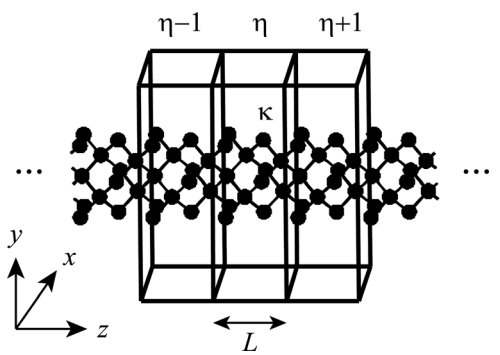

FIG. 2. Schematic diagram representing the atomic index κ and unit cells. The position of the Si atom is identified using the atomic index κ and the unit cell index η as (η, κ). L is the length of the unit cell in the transport direction.

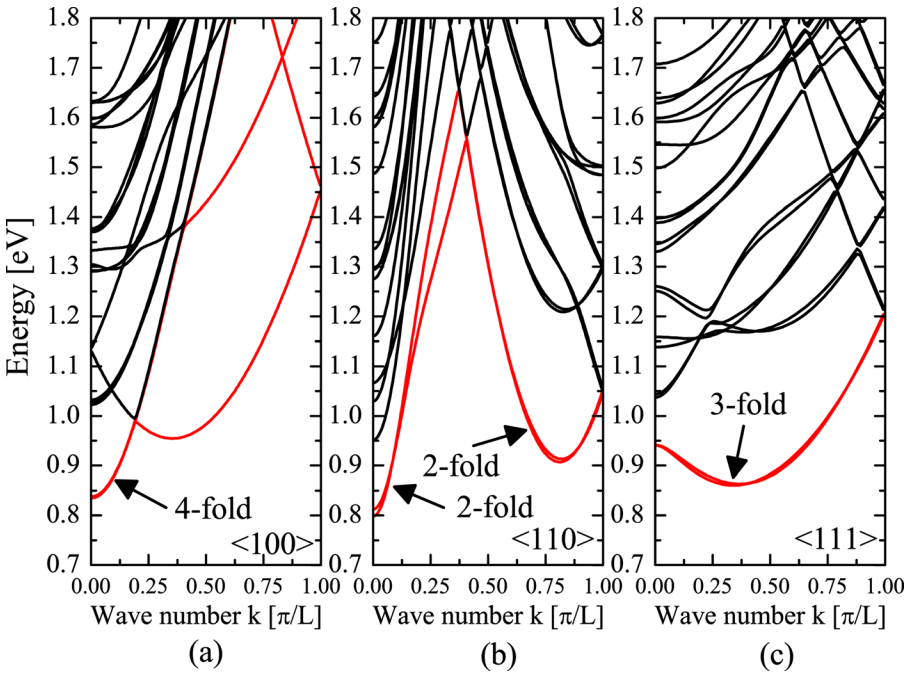

FIG. 3. Electron band structures computed for (a) ⟨100⟩-, (b) ⟨110⟩-, and (c) ⟨111⟩-oriented Si nanowires with diameters of approximately 3 nm. The red lines denote conduction bands used in the mobility calculation.

elements of triangular matrices that were smaller than a predetermined threshold were omitted.

Figure 3 shows the electron band structures computed for (a) ⟨100⟩-oriented, (b) ⟨110⟩-oriented, and (c) ⟨111⟩-oriented Si nanowires with diameters of about 3 nm, where the horizontal axis denotes the wavenumber normalized by the Brillouin zone width in each case. The origin of the vertical axis, i.e., $E = 0$, corresponds to the Fermi level. For the ⟨100⟩- and ⟨110⟩-oriented Si nanowires, the conduction band minimum appears at the Γ point, while it appears away from the Γ point for the ⟨111⟩-orientation. Also, the lowest subbands are nearly degenerate, as indicated in each figure. The differences in the band structures among these orientations, including the number of degeneracies, can be qualitatively explained in terms of the two-dimensional quantum confinement of the six equivalent ellipsoidal valleys in bulk Si.[19,20] Next, Fig. 4 shows the transport effective mass at the conduction band minimum as a function of the diameter for the three orientations. Note that the horizontal dashed lines represent the bulk effective masses corresponding to the ⟨100⟩- and ⟨110⟩-orientations, which are both $m_t = 0.19m_0$, and corresponding to the ⟨111⟩-orientation, which is $(2m_t + m_l)\ /3 = 0.43m_0$.[21] It is found that the transport masses of the ⟨100⟩- and ⟨111⟩-orientations increase from the bulk value as the diameter decreases. In contrast, the transport mass of the ⟨110⟩-orientation decreases from the bulk value. The transport effective mass behavior is caused by the two-dimensional quantization of the anisotropic and nonparabolic Si conduction band.[19,20] Therefore, intuitively, higher electron mobility can be expected in ⟨110⟩-oriented Si nanowires with a nanometer-sized cross-section. We discuss this point later in Sec. IV.

B. Phonons

Phonon band structures were computed using the original Keating valence force field (VFF) approach,[13] which is known to describe the microscopic features of phonon eigenstates in nanostructures well.

The Keating potential consists of two potential energy terms: the first is the bond-stretching term, and the other is the bond-bending term. Each term is represented as a function of the atomic coordinates, and for a diamond structure, the crystal potential energy (Keating potential energy) is given by

$$E = \frac{3}{16}\frac{\alpha}{d_1^2}\sum_{\eta,\kappa}\sum_{(\eta',\kappa')\in NN(\eta,\kappa)}\left(R^2_{\eta\kappa,\eta'\kappa'} - d_1^2\right)^2 + \frac{3}{16}\frac{\beta}{d_1^2}\sum_{\eta,\kappa}\sum_{(\eta',\kappa')\in NN(\eta\kappa)}\sum_{\substack{(\eta'',\kappa'')\in NN(\eta,\kappa)\\ \eta''\neq\eta'\cap\kappa''\neq\kappa'}}\left(\mathbf{R}_{\eta\kappa,\eta'\kappa'}\cdot\mathbf{R}_{\eta\kappa,\eta''\kappa''} + \frac{1}{3}d_1^2\right)^2. \quad (4)$$

Here, the first and the second terms correspond to the bond-stretching and bond-bending terms, respectively, and α and β are Keating's force constants. $NN(\eta,\kappa)$ stands for a group of nearest-neighbor atoms associated with the (η,κ) th atom. $\mathbf{R}_{\eta\kappa,\eta'\kappa'} = \mathbf{R}_{\eta'\kappa'} - \mathbf{R}_{\eta\kappa}$ indicates the relative position vector between the two atoms and d_1 is the equilibrium bond length

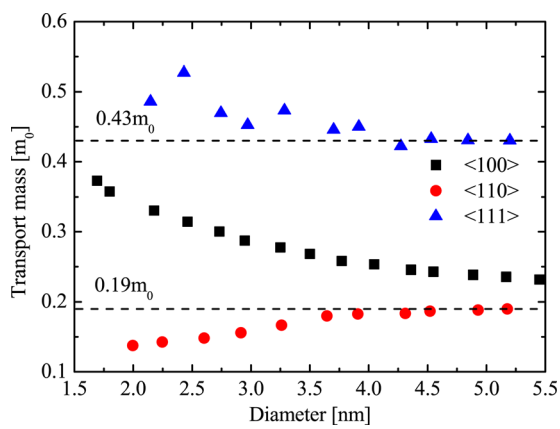

FIG. 4. Transport effective mass at the conduction band minimum as a function of the diameter for the three crystalline orientations, where the horizontal dashed lines represent bulk effective masses corresponding to each orientation.

between nearest neighbor Si atoms. In the Keating VFF approach, the phonon band structures are calculated by introducing a harmonic perturbation approximation into Eq. (4). If all atoms are fixed to their equilibrium positions $(\mathbf{R}_1^0, \mathbf{R}_2^0, \ldots, \mathbf{R}_N^0)$, the potential energy and forces acting on the atoms are found to be all zero from Eq. (4). This means that $E(\mathbf{R}_1^0, \mathbf{R}_2^0, \ldots, \mathbf{R}_N^0) \equiv E_0 = 0$ and $\nabla_{\mathbf{R}_i} E(\mathbf{R}_1, \mathbf{R}_2, \ldots, \mathbf{R}_N)\big|_{\mathbf{R}=\mathbf{R}_1^0, \mathbf{R}_2^0, \ldots, \mathbf{R}_N^0} (i \in 1, 2, \ldots, N) = 0$. Therefore, Eq. (4) is expanded using higher-order spatial derivatives, and when we ignore the components that are higher than the third-order, the Keating potential energy is finally given by

$$\begin{aligned} E &= E_0 + \sum_{\eta\kappa} \sum_{\mu\in\{x,y,z\}} \left.\frac{\partial E}{\partial R_{\eta\kappa\mu}}\right|_0 \delta R_{\eta\kappa\mu} \\ &\quad + \frac{1}{2} \sum_{\eta\kappa} \sum_{\mu\in\{x,y,z\}} \sum_{\eta'\kappa'} \sum_{\mu'\in\{x,y,z\}} \left.\frac{\partial^2 E}{\partial R_{\eta\kappa\mu} \partial R_{\eta'\kappa'\mu'}}\right|_0 \delta R_{\eta\kappa\mu} \delta R_{\eta'\kappa'\mu'} + \ldots \\ &\approx \frac{1}{2} \sum_{\eta\kappa} \sum_{\mu\in\{x,y,z\}} \sum_{\eta'\kappa'} \sum_{\mu'\in\{x,y,z\}} \left.\frac{\partial^2 E}{\partial R_{\eta\kappa\mu} \partial R_{\eta'\kappa'\mu'}}\right|_0 \delta R_{\eta\kappa\mu} \delta R_{\eta'\kappa'\mu'}, \end{aligned} \tag{5}$$

where μ denotes three Cartesian coordinates $\{x,y,z\}$, and $\delta R_{\eta\kappa\mu}$ denotes infinitesimal displacements from the equilibrium position of the (η,κ) th atom.

By applying Eq. (5) to Newton's equation of motion, we obtained a dynamical equation for the atomic displacement $\delta R_{\eta\kappa\mu}$ of the (η,κ) th atom, as follows:

$$M \frac{\partial^2 \delta R_{\eta\kappa\mu}}{\partial t^2} = -\sum_{\eta',\kappa'} \sum_{\nu\in\{x,y,z\}} \left.\frac{\partial^2 E}{\partial R_{\eta\kappa\mu} \partial R_{\eta'\kappa'\mu'}}\right|_0 \delta R_{\eta'\kappa'\mu'}, \tag{6}$$

where M denotes the mass of the Si atom. The factor 1/2 of Eq. (5) was canceled out by the symmetry in the suffixes. Here, we assume a solution for the atomic vibration in the form of a plane wave along the transport direction, such as $\delta R_{\eta\kappa\mu} \propto e^{i(qz-\omega t)}$, and consequently the following dynamical matrix equation has been derived:

$$\begin{aligned} &\sum_{(\eta',\kappa')\in NN(\eta,\kappa)} \sum_{\mu\in\{x,y,z\}} D^1_{\eta\kappa\mu,\eta'\kappa'\mu'} [\varepsilon^\lambda_{\kappa'\mu'}(q) e^{iq(\eta'-\eta)L} - \varepsilon^\lambda_{\kappa\mu'}(q)] \\ &\quad + \sum_{(\eta',\kappa')\in NN(\eta,\kappa)} \sum_{\substack{(\eta'',\kappa'')\in NN(\eta',\kappa') \\ \eta''\neq\eta\cap\kappa''\neq\kappa}} \sum_{\mu''\in\{x,y,z\}} D^2_{\eta\kappa\mu,\eta'\kappa',\eta''\kappa''\mu''} [\varepsilon^\lambda_{\kappa''\mu''}(q) e^{iq(\eta''-\eta)L} - \varepsilon^\lambda_{\kappa\mu''}(q)] = \omega^2_\lambda(q) \varepsilon^\lambda_{\kappa\mu}(q), \end{aligned} \tag{7}$$

where ε and ω are eigenvectors and eigenvalues for the phonons. In Eq. (7), $D^1_{\eta\kappa\mu,\eta'\kappa'\mu'}$ and $D^2_{\eta\kappa\mu,\eta'\kappa',\eta''\kappa''\mu''}$ are matrix elements between the first nearest-neighbor and the second nearest-neighbor Si atoms, respectively, which are represented by

$$\begin{aligned} D^1_{\eta\kappa\mu,\eta'\kappa'\mu'} &= -3\frac{\alpha}{d_1^2} \frac{R^\mu_{\eta\kappa,\eta'\kappa'} R^{\mu'}_{\eta\kappa,\eta'\kappa'}}{\sqrt{M_\kappa M_{\kappa'}}} \\ &\quad - \frac{3}{4}\frac{\beta}{d_1^2} \sum_{\substack{(\eta'',\kappa'')\in NN(\eta,\kappa) \\ \eta''\neq\eta'\cap\kappa''\neq\kappa'}} \frac{(R^\mu_{\eta\kappa,\eta'\kappa'} + R^\mu_{\eta\kappa,\eta''\kappa''}) R^{\mu'}_{\eta\kappa,\eta''\kappa''}}{\sqrt{M_\kappa M_{\kappa'}}} \\ &\quad - \frac{3}{4}\frac{\beta}{d_1^2} \sum_{\substack{(\eta'',\kappa'')\in NN(\eta',\kappa') \\ \eta''\neq\eta\cap\kappa''\neq\kappa}} \frac{R^\mu_{\eta'\kappa',\eta''\kappa''} (R^{\mu'}_{\eta'\kappa',\eta\kappa} + R^{\mu'}_{\eta'\kappa',\eta''\kappa''})}{\sqrt{M_\kappa M_{\kappa'}}}, \end{aligned} \tag{8}$$

$$D^2_{\eta\kappa\mu,\eta'\kappa',\eta''\kappa''\mu''} = \frac{3}{4}\frac{\beta}{d_1^2} \frac{R^\mu_{\eta'\kappa',\eta''\kappa''} R^{\mu''}_{\eta'\kappa',\eta\kappa}}{\sqrt{M_\kappa M_{\kappa''}}}. \tag{9}$$

In Eqs. (8) and (9), $R^\mu_{\eta\kappa,\eta'\kappa'}$ is the directional component of the relative position vectors from (η,κ) to the (η',κ') th atoms. We note that the bond-stretching term (the first term in Eq. (4)) is involved only in $D^1_{\eta\kappa\mu,\eta'\kappa'\mu'}$, while the bond-bending term (the second term in Eq. (4)) is involved in both $D^1_{\eta\kappa\mu,\eta'\kappa'\mu'}$ and $D^2_{\eta\kappa\mu,\eta'\kappa',\eta''\kappa''\mu''}$. Therefore, the dynamical matrix for a specified atom contains up to 4 coupling elements with the first nearest-neighbor atoms, and up to 12 coupling elements with the second nearest-neighbor atoms. As a matter of course, these matrix elements depend on the cross-sectional geometry and the crystal orientations of the nanowires. By solving Eq. (7) using the matrix elements defined by Eqs. (8) and (9), the phonon band structure can be obtained.

In practical calculations, we used prescribed force constants for the bond-stretching term α and the bond-bending term β. Although the dynamical matrix is also Hermitian and positive definite, we have calculated all eigenvalues and eigenvectors using the LAPACK library,[22] because the electron-phonon scattering rates formulated in the next section must be estimated for the entire first Brillouin zone. The phonon band structures were calculated in the absence of the gate dielectric and the metallic gate, and the surface Si atoms were assumed to be freely-vibrating.

Figure 5 shows the phonon band structures computed for the three orientations in the low energy regime, where the diameter is approximately 3 nm and the horizontal axis denotes the normalized phonon wavenumber. Unlike in bulk phonons, four acoustic modes exist in a long wavelength regime,[23] i.e., $q \approx 0$. We symbolize these modes as TLA1, TLA2, TA, and LA from the bottom up, as shown in Fig. 5, where TA and LA are the transverse acoustic and longitudinal acoustic modes, respectively, in common with the bulk phonon, and TLA is a mixed state of transverse and longitudinal acoustic modes. By looking closely at these four curves, we notice that TLA1 and TLA2 are degenerate in the $\langle 100\rangle$- and $\langle 111\rangle$-orientations, while they are non-degenerate in the $\langle 110\rangle$-orientation. This is because of the presence or absence of rotational symmetry. Specifically, the $\langle 100\rangle$- and

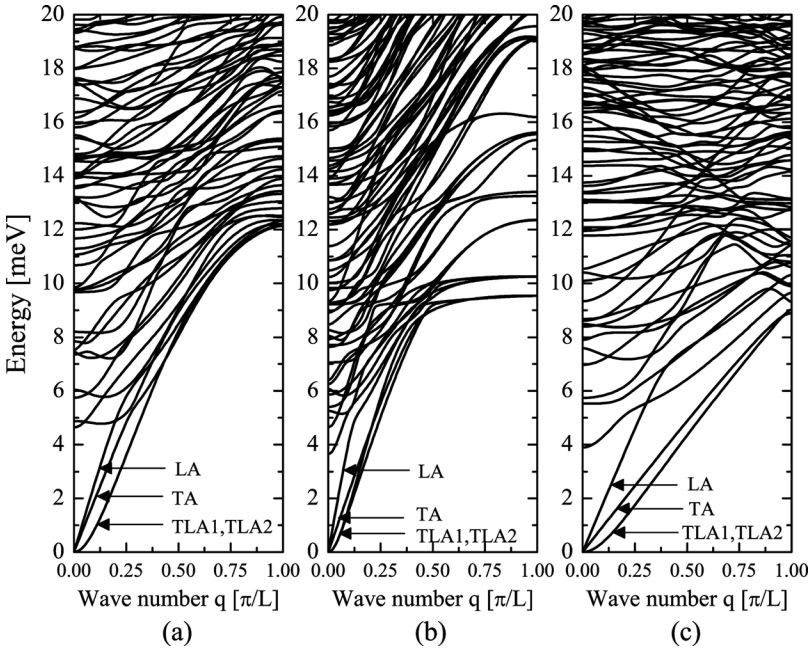

FIG. 5. Phonon band structures computed for (a) ⟨100⟩-, (b) ⟨110⟩-, and (c) ⟨111⟩-oriented Si nanowires in a low energy regime, where the diameter is about 3 nm. Unlike bulk phonons, four acoustic modes exist in the long wavelength regime, i.e., $q \approx 0$. We symbolize these modes as TLA1, TLA2, TA, and LA from the bottom upwards.

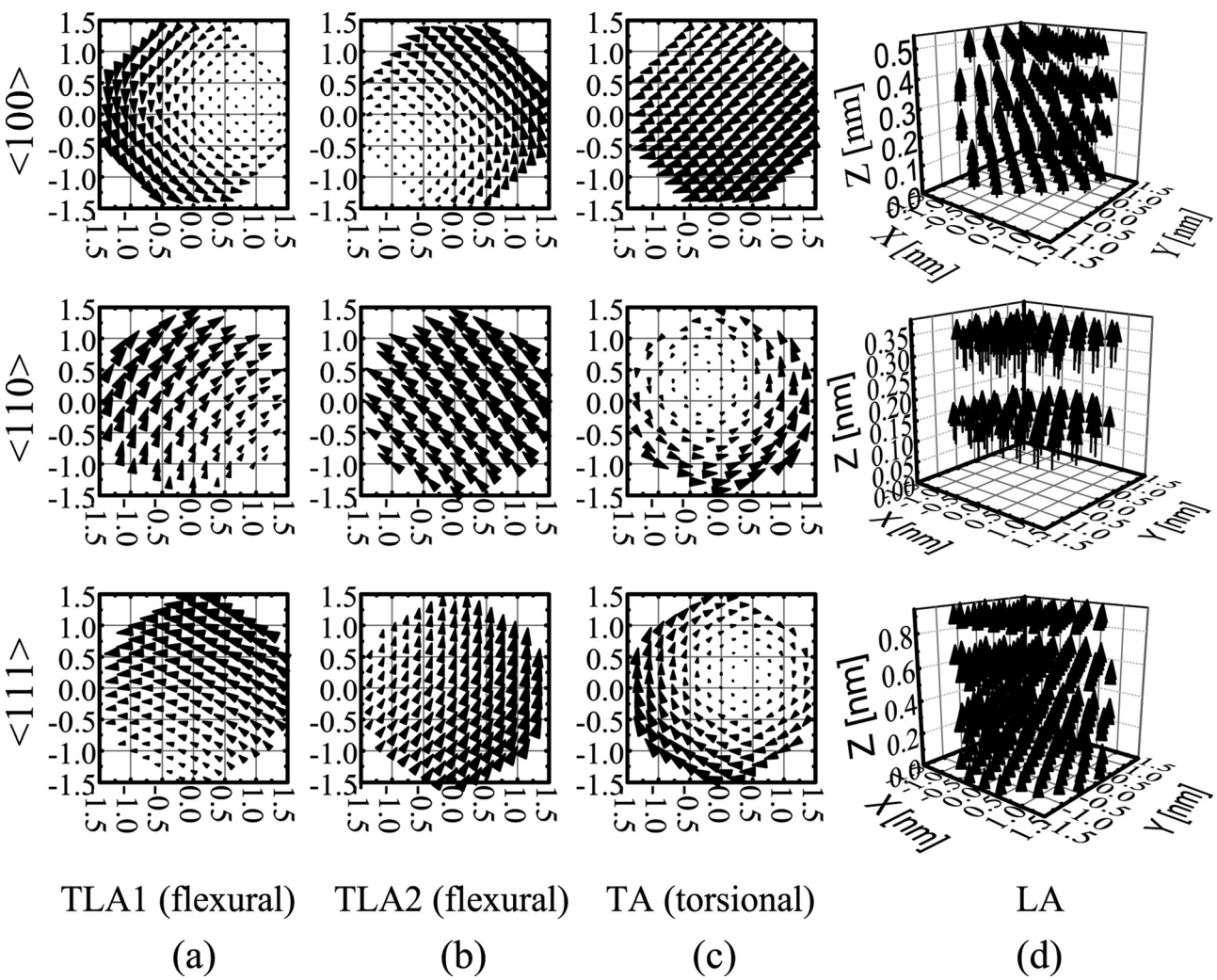

FIG. 6. Atomic vibration vectors at $q = 0$ of four acoustic phonon modes computed for the three crystalline orientations. (a) and (b) are flexural modes, (c) is a torsional mode, and (d) is the LA mode. The diameter is about 3 nm. Si atoms are located at the origin of each glyph.

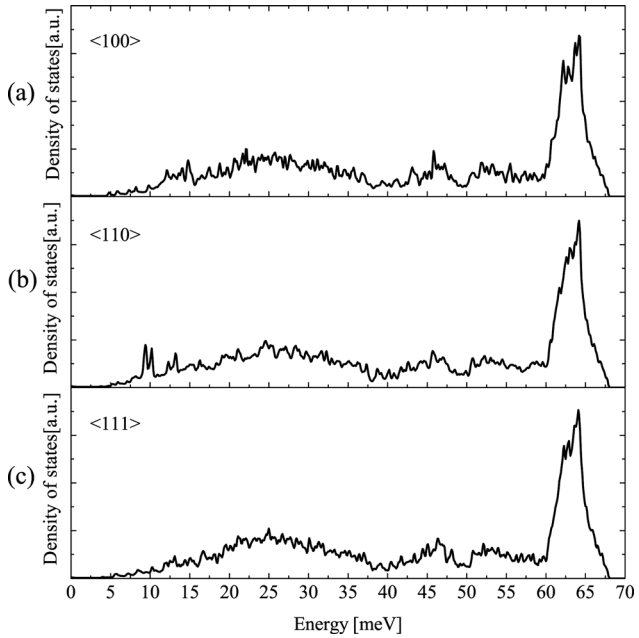

FIG. 7. Phonon density-of-states computed for (a) ⟨100⟩-, (b) ⟨110⟩-, and (c) ⟨111⟩-oriented Si nanowires with diameters of about 3 nm.

⟨111⟩-oriented Si nanowires have rotational symmetries of π and $2\pi/3$, respectively, but the ⟨110⟩-oriented nanowire has no rotational symmetry. Therefore, the TLA1 and TLA2 modes become non-degenerate in the ⟨110⟩-orientation. This can also be confirmed by actually plotting the atomic vibration vectors at the limit of $q=0$. Figure 6 shows the atomic vibration vectors of the four acoustic phonon modes computed for the three orientations. For the ⟨100⟩- and ⟨111⟩-orientations, the TLA1 and TLA2 modes exhibit identical vibration patterns considering each rotational symmetry mentioned above. However, the ⟨110⟩-oriented nanowire clearly has different vibration patterns between the TLA1 and TLA2 modes, which means that the rotational symmetry is absent in this orientation. Incidentally, from the vibration patterns shown in Fig. 6, the TLA1 and TLA2 modes are named "flexural" and the TA mode is called "torsional." Also, as found in Fig. 5, the two flexural modes exhibit $\omega \propto q^2$ dispersions, while the torsional mode has a $\omega \propto q$ dispersion, which is the nature of a purely transverse mode.

Next, we investigated another phonon property in Si nanowires. Figure 7 shows the phonon densities-of-states obtained for Si nanowires with the three orientations and diameters of about 3 nm. First, it is found that the densities-of-states are sharply-peaked around 65 meV for all the orientations, which is because of the optical phonon modes. It is interesting that the vibrational energies of the optical phonon modes in Si nanowires remain similar to those of bulk Si.[6] On the other hand, broad peaks extending from ~10 meV to ~40 meV result from mixed states of the acoustic and optical phonons. We should also note that the apparent difference caused by the nanowire orientation is visually unrecognizable in the present density-of-states.

Sound velocities are evaluated from the phonon band structures at $q \approx 0$ of Fig. 5, and are plotted as a function of diameter in Fig. 8. The data for TA and LA represent the sound velocities for the TA and LA modes in Fig. 5, respectively, and those of the TLA modes are not shown here. The horizontal dashed lines indicate the theoretical sound velocities for the TA and LA modes in bulk Si.[24] It is found that as the diameter decreases, the sound velocities decrease because of the phonon confinement effect. Also, we note that the calculated sound velocities depend on the crystalline orientation, and their magnitude relation corresponds well to that of bulk Si, especially in a larger diameter regime. Consequently, the phonon confinement and anisotropic effects in Si nanowires are considered to be successfully described by the present Keating potential approach.

III. ELECTRON-PHONON INTERACTION

In this section, we formulate the scattering rates caused by electron-phonon interaction in the Si nanowires by coupling the electron and phonon eigenstates derived in Sec. II.

First, we represent the atomic position vector $\mathbf{R}_{\eta\kappa}(t)$ by adding an atomic vibration vector $\delta\mathbf{R}_{\eta\kappa}(t)$ to the equilibrium position vector $\mathbf{R}^0_{\eta\kappa}$ as follows:

$$\mathbf{R}_{\eta\kappa}(t) = \mathbf{R}^0_{\eta\kappa} + \delta\mathbf{R}_{\eta\kappa}(t). \tag{10}$$

Here, we define the atomic vibration vector in the second quantization notation as

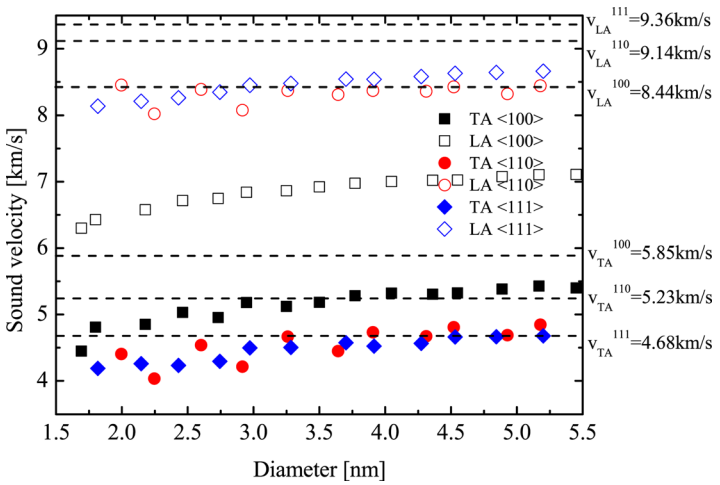

FIG. 8. Sound velocities of TA and LA phonon modes at $q \approx 0$ for the three crystalline orientations. The horizontal dashed lines indicate theoretical sound velocities for the TA and LA modes in bulk Si.

$$\delta\mathbf{R}_{\eta\kappa}(t) = \sum_{q,\lambda} \sqrt{\frac{\hbar}{2MN\omega_\lambda(q)}} \left[a_{q\lambda}\varepsilon_\kappa^\lambda(q) e^{i\left(q\eta L - \omega_\lambda(q)t\right)} + a_{q\lambda}^* \varepsilon_\kappa^{\lambda *}(q) e^{-i\left(q\eta L - \omega_\lambda(q)t\right)} \right], \tag{11}$$

where $a_{q\lambda}$ and $a_{q\lambda}^*$ are the phonon annihilation and creation operators, respectively. $\varepsilon_\kappa^\lambda(q)$ is the eigenvector of the (η,κ) th atom at the wavevector q and the λth branch. When the electron-phonon interaction Hamiltonian is represented by the $sp^3d^5s^*$ orbitals and is expanded to a first-order spatial derivative term as[25]

$$U_{\eta\kappa,\eta'\kappa'}^{\gamma,\gamma'}(\mathbf{R}_{\eta\kappa},\mathbf{R}_{\eta'\kappa'}) \approx U_{\eta\kappa,\eta'\kappa'}^{\gamma,\gamma'}(\mathbf{R}_{\eta\kappa}^0,\mathbf{R}_{\eta'\kappa'}^0) + \left.\frac{\partial U_{\eta\kappa,\eta'\kappa'}^{\gamma,\gamma'}}{\partial(\mathbf{R}_{\eta'\kappa'}-\mathbf{R}_{\eta\kappa})}\right|_0 \bullet [\delta\mathbf{R}_{\eta'\kappa'}(t) - \delta\mathbf{R}_{\eta\kappa}(t)], \tag{12}$$

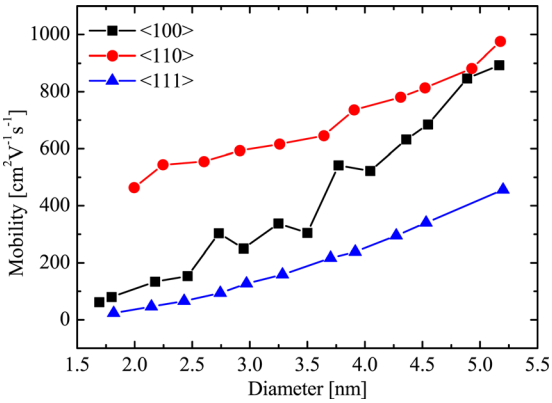

FIG. 9. Computed electron mobilities of Si nanowires for three crystalline orientations as a function of diameter.

then the transition matrix element from a state (n,k) to a state (n',k') is given by

$$\mathcal{M}^{n,n'}(k,k') = \sum_{q,\lambda} \sqrt{\frac{\hbar}{2MN\omega_\lambda(q)}} \sum_\kappa \sum_{\eta',\kappa'\in NN(\eta,\kappa)} \sum_\gamma \sum_{\gamma'} \left.\frac{\partial U_{\eta\kappa,\eta'\kappa'}^{\gamma,\gamma'}}{\partial(\mathbf{R}_{\eta'\kappa'}-\mathbf{R}_{\eta\kappa})}\right|_0 \times \begin{bmatrix} \varepsilon_{\kappa',\lambda}(\pm q) c_{\kappa,\gamma}^{n'*}(k') c_{\kappa',\gamma'}^{n}(k) e^{ik'(\eta'-\eta)L} \\ -\varepsilon_{\kappa,\lambda}(\pm q) c_{\kappa,\gamma}^{n'*}(k') c_{\kappa',\gamma'}^{n}(k) e^{ik(\eta'-\eta)L} \end{bmatrix} \delta_{k-k'\pm q,G} e^{-i[E_n(k)/\hbar - E_{n'}(k')/\hbar \pm \omega_\lambda(q)]t}. \tag{13}$$

In practical calculations, solutions for the electron wavefunctions $c(k)$ and the phonon eigenvalues $\omega(q)$ and polarization vectors $\varepsilon(q)$, which have been derived in Sec. II, are substituted into Eq. (13). However, the electron eigenenergies are implicitly considered in the term $\partial U_{\eta\kappa,\eta'\kappa'}^{\gamma,\gamma'}/\partial(\mathbf{R}_{\eta'\kappa'}-\mathbf{R}_{\eta\kappa})$, which is numerically calculated using analytical formulae given by the Slater-Koster table, as described in Appendix B.

Note that G denotes the reciprocal lattice vector, and thus both normal ($G=0$) and umklapp ($G\neq 0$) processes caused by the phonon scattering are automatically included in the present calculation.

Next, the scattering rates from state (n,k) to state (n',k') are represented by applying Fermi's golden rule as follows:

$$S^{n,n'}(k,k') = \frac{2\pi}{\hbar} \begin{bmatrix} |\mathcal{M}^{n,n'}(k,k')|^2 g\left(\hbar\omega_\lambda(k'-k)\right) \delta\left(E_n(k) - E_{n'}(k') + \hbar\omega_\lambda(k'-k)\right) \\ +|\mathcal{M}^{n,n'}(k,k')|^2 [1+g\left(\hbar\omega_\lambda(k-k')\right)] \delta\left(E_n(k) - E_{n'}(k') - \hbar\omega_\lambda(k-k')\right) \end{bmatrix}, \tag{14}$$

where $g\left(\hbar\omega_\lambda(q)\right)$ is the equilibrium Bose-Einstein distribution function, and the Dirac delta function represents the energy conservation law. Here, as found from Eq. (14), the final states (n',k') after the scattering events need to be searched by imposing momentum and energy conservations. To perform accurate detection of the final states over the whole of the first Brillouin zone, we introduced quadratic spline interpolations of the electron and phonon band structures between discretized points. Also, to realize a more rigorous estimation of the joint density-of-states involving the group velocities of both electrons and phonons at the final states, we transformed the Dirac delta function in Eq. (14) by using a mathematical formula as follows:

$$\delta\left(E_n(k) - E_{n'}(k') \pm \hbar\omega(\pm k' \mp k)\right) = \sum_i \frac{1}{\left|\frac{\partial[E_{n'}(k') \mp \hbar\omega_\lambda(\pm k' \mp k)]}{\partial k'}\right|_{k'=k_i}} \delta(k'-k_i). \tag{15}$$

These approaches enable us to perform numerically stable and accurate estimation of the scattering rates.

IV. ELECTRON MOBILITY CALCULATION

Next, we describe a methodology to compute the electron mobility. By assuming that the electron distribution function $f_n(k)$ can be represented by the sum of the

equilibrium Fermi-Dirac function $f_0(E_n(k))$ and a first-order perturbation component $\delta f_n(k)$ driven by an electric field F, the following equation is derived from the Boltzmann transport equation:[26]

$$-\frac{e}{k_B T}Fv_n(k)f_0\Big(E_n(k)\Big)\Big[1-f_0\Big(E_n(k)\Big)\Big]=\hat{C}\{\delta f_n(k)\}, \tag{16}$$

where $v_n(k)=\partial E_n(k)/\hbar\partial k$ is the group velocity of the electrons, which is calculated using the electron band structure, and T is the temperature. For the calculations in this paper, we estimated the electron mobility at room temperature. Next, we represented the collisional integral in the right-hand side of Eq. (16) using the scattering rate $S^{n,n'}(k,k')$ and applying detailed balance conditions. As a result, we obtained the following expression for the collisional integral:

$$\hat{C}\{\delta f_n(k)\}=\frac{NL}{2\pi}\sum_{n'}\int_{-\pi/L}^{\pi/L}dk' S^{n,n'}(k,k')\left[\delta f_{n'}(k')\frac{f_0(E_n(k))}{f_0(E_{n'}(k'))}-\delta f_n(k)\frac{1-f_0(E_{n'}(k'))}{1-f_0(E_n(k))}\right]. \tag{17}$$

Here, L denotes the length of the unit cell in the transport direction and N is the number of the unit cells. The first and second terms correspond to the in-scattering process from (n',k') to (n,k) and the out-scattering process from (n,k) to (n',k'), respectively. We introduce a relaxation time approximation,

$$\hat{C}\{\delta f_n(k)\}=-\frac{\delta f_n(k)}{\tau_n(k)}. \tag{18}$$

Then, by substituting Eq. (18) into Eq. (17), the relaxation time $\tau_n(k)$ is calculated by numerically solving the following integral equation:

$$\frac{NL}{2\pi}\sum_{n'}\int_{-\pi/L}^{\pi/L}dk' S^{n,n'}(k,k')\frac{1-f_0\Big(E_{n'}(k')\Big)}{1-f_0\Big(E_n(k)\Big)}\times[v_n(k)\tau_n(k)-v_{n'}(k')\tau_{n'}(|k'|)]=v_n(k). \tag{19}$$

It should be emphasized that Pauli's exclusion principle is strictly taken into account in Eq. (19). Because the relaxation time is an even function of k, i.e., $\tau_n(k)=\tau_n(-k)$, we only need to solve Eq. (19) in a half-space of the first Brillouin zone, e.g., $k\in[0,\pi/L]$.

Once the relaxation time was obtained, electronic conductivity σ can be calculated using the following equation:[27,28]

$$\sigma=\sum_n\frac{4e^2}{2\pi k_B T}\int_0^{\pi/L}dk\Big(v_n(k)\Big)^2\tau_n(k)f_0\Big(E_n(k)\Big)\times\Big[1-f_0\Big(E_n(k)\Big)\Big]. \tag{20}$$

Finally, we compute the electron density in the conduction band by using

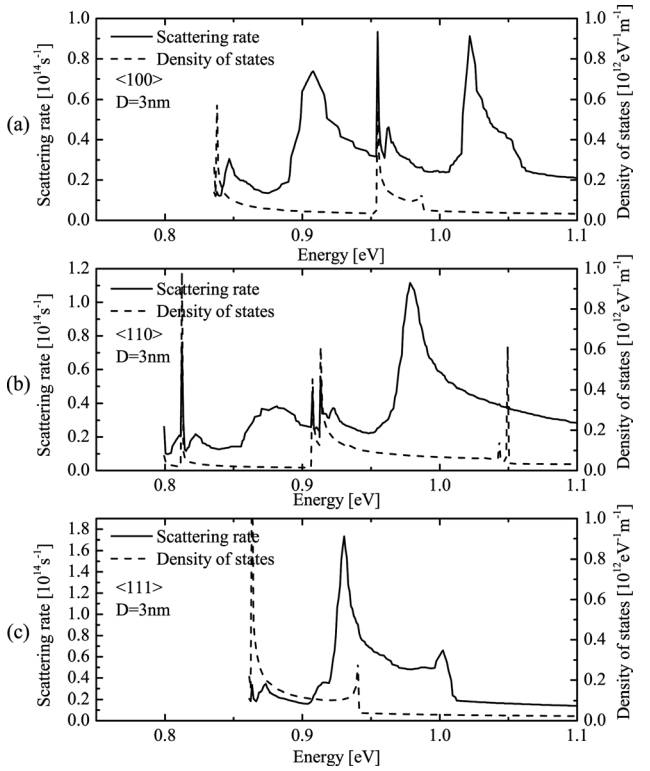

FIG. 10. Total scattering rates computed for (a) ⟨100⟩-, (b) ⟨110⟩-, and (c) ⟨111⟩-oriented Si nanowires with diameters of about 3 nm. The solid lines represent the total scattering rates and the dashed lines represent the density-of-states for the electrons.

$$n=\sum_n\frac{4}{2\pi}\int_0^{\pi/L}dkf_0\Big(E_n(k)\Big), \tag{21}$$

and the electron mobility μ is evaluated from the relationship $\sigma=en\mu$. The number of conduction subbands necessary for accurate mobility estimation depends on the wire orientation, and thus the conduction subbands used in the actual simulation are highlighted by the red lines in Fig. 3. The inclusion of these subbands is considered to be sufficient because the higher subbands are located away from them by more than the thermal energy at room temperature for the present diameter range (D<5 nm), and also because the gate voltage was set at zero.

The computed electron mobilities are shown in Fig. 9 as a function of the diameter. It is found that the electron mobilities significantly decrease with decreasing diameter, which suggests that the electron-phonon interaction becomes stronger. To examine this point, we plot the total scattering rates for a diameter (D) of about 3 nm in Fig. 10 and for D of about 4.5 nm in Fig. 11, which were calculated using the following equation:[29]

$$\frac{1}{\tau(E)}=\left(\sum_{n,n'}\int\int_{-\pi/L}^{\pi/L}dkdk' S^{n,n'}(k,k')\frac{1-f_0\Big(E_{n'}(k')\Big)}{1-f_0\Big(E_n(k)\Big)}\times\delta\Big(E-E_n(k)\Big)\right)\Big/\sum_n\int_{-\pi/L}^{\pi/L}dk\delta\Big(E-E_n(k)\Big). \tag{22}$$

Note that all scattering processes including TA, LA, TLA, and optical phonon modes are considered. It was found that the total scattering rate increases with decreasing diameter for all of the orientations, as expected. Here, to explain the complicated behavior of the scattering rates, we also plotted the density-of-states for the electrons in the dashed lines. First, a peak is found at each Van Hove singularity point, which indicates that the one-dimensional nature of the Si nanowires is described well. Also, a small but broad peak appears right next to each singularity point, which is caused by the excitation of acoustic phonons at the Brillouin zone boundary. An extensive broad peak caused by optical phonon emission, where the electrons need to have greater kinetic energies than the optical phonon energies of ~65 meV, is also clearly observed above each singularity point.

We now take particular note of the total scattering rates around the conduction band minima, which are governed by intrasubband acoustic phonon scattering and determine the electron mobility. A closer look reveals that the scattering rates exhibit similar values among the three orientations, except at the Van Hove singularity points, which is true for both diameters. The rates are approximately 1×10^{13} s^{-1} for $D = 4.5$ nm and approximately 2×10^{13} s^{-1} for $D = 3.0$ nm. As a result, the electron mobilities decrease with decreasing diameter, as shown in Fig. 9. It should be noted here that the scattering rate has two contributions from the transition matrix element $|\mathcal{M}^{n,n'}(k,k')|^2$ and the density-of-states, as represented in Eq. (14). We next examine the density-of-states for the electrons plotted in Figs. 10 and 11 in more detail.

Looking at the curves for the density-of-states in Figs. 10 and 11 carefully, we find that they vary in accordance with the orientation and diameter dependencies of the effective mass shown in Fig. 4. More specifically, the density-of-states around the conduction band minima increases with decreasing diameter for the ⟨100⟩- and ⟨111⟩-orientations because of the increased effective mass, while it decreases for the ⟨110⟩-orientation because of the decreased effective mass. The density-of-states for the ⟨110⟩-orientation is also found to be smaller than that of the other two orientations because of its smaller effective mass for both diameters. Nevertheless, the total scattering rates are found to be similar among the three orientations, which means that the transition matrix element is larger for the ⟨110⟩-orientation as compared to the others. This is consistent with the results from elastic simulation for strained-Si, i.e., variation of the conduction band minimum because of uniaxial strain, which corresponds to the magnitude of the deformation potential, is larger along the ⟨110⟩-orientation than along the ⟨100⟩-orientation.[20,30] To summarize the above discussion, the total scattering rates responsible for the mobility are nearly constant among the three orientations, as a consequence of a fortuitous balance of the influences of the density-of-states for electrons and the transition matrix element.

Because we considered the diameter-dependent and anisotropic electron-phonon interaction, the mobility for the ⟨110⟩-orientation in our results monotonically decreases with decreasing diameter. However, in previous simulations[9] of atomistic electron band structures computed using the sp^{3}d^{5}s* TB approach and using diameter-independent bulk phonons, the ⟨110⟩-orientation exhibits a constant mobility at around 700 cm^2/(V·s) for diameters less than 5 nm. We consider such a discrepancy to be because of the difference in the theoretical treatment of the phonons. However, the phonon-limited mobilities reported in Ref. 9 indicate a similar magnitude relationship to our results.

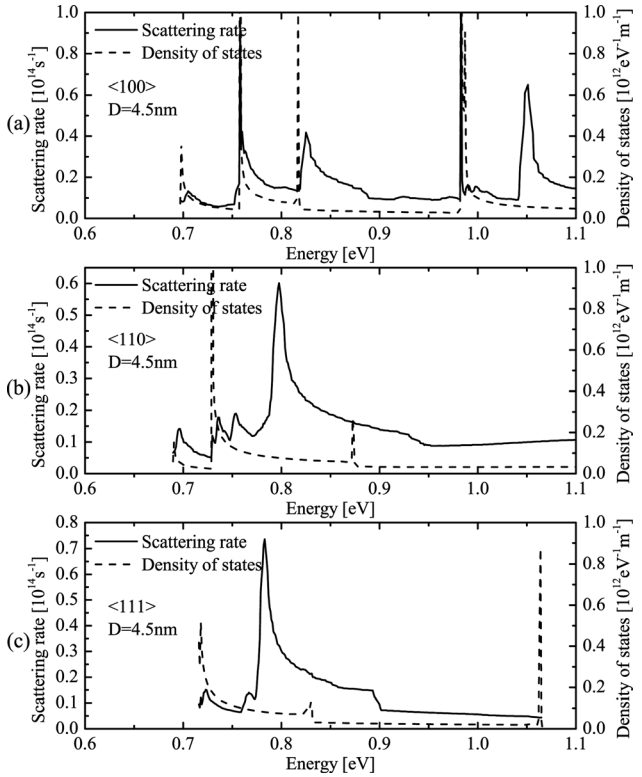

FIG. 11. Total scattering rates computed for (a) ⟨100⟩-, (b) ⟨110⟩-, and (c) ⟨111⟩-oriented Si nanowires with diameters of about 4.5 nm. The solid lines represent the total scattering rates and the dashed lines represent the density-of-states for the electrons.

In Fig. 9, the ⟨110⟩-oriented Si nanowires show the highest electron mobility in the present range of diameters, while the ⟨111⟩-oriented nanowires show the lowest. This trend is the same as that in Ref. 9, and therefore the wire-orientation dependence of the electron mobility is primarily governed by the difference between the electron effective masses, as shown in Fig. 4. Specifically, the ⟨110⟩-orientation exhibits the smallest effective mass, and the ⟨111⟩-orientation has the largest, which corresponds to the relative magnitude relationship in the electron mobilities. This is also supported by the fact that the electron mobilities of the ⟨100⟩- and ⟨110⟩-orientations approach each other as the diameter increases to 5 nm, which agrees well with the variation in the effective mass. Accordingly, the effective mass of the electrons plays a primary role in determining the atomistic electron mobility of the Si nanowires. From another point of view, the qualitative trend in the electron mobility can be understood by considering the atomistic band structures of the electrons. The present results also suggest that the ⟨110⟩-orientation is promising for high-performance Si nanowire MOSFETs with diameters of less than 5 nm.

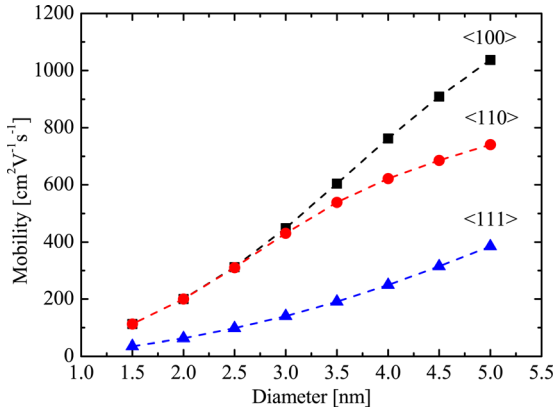

FIG. 12. Computed electron mobilities of the Si nanowires using diameter-independent isotropic deformation potentials and self-consistent Schrödinger-Poisson solutions.

Finally, we compare our atomistic electron mobilities with those calculated by an approach based on an analytical effective mass and a simple isotropic deformation potential. Figure 12 shows the electron mobilities as a function of diameter calculated using the formulation of the effective mass in Ref. 21 and diameter-independent isotropic deformation potentials,[3,5] where the value of the deformation potential for acoustic phonons was given as 12 eV according to Ref. 3 and the parameter set for intervalley scattering was taken from Ref. 6. Electronic subband structures were calculated by solving the two-dimensional Schrödinger and Poisson equations self-consistently.[3] The degradation behavior of the electron mobility with decreasing diameter is similar to that in Fig. 9, but the magnitude relationship between the $\langle 100 \rangle$- and $\langle 110 \rangle$-orientations is reversed, which is mainly because the electron band structures, i.e., the electron effective masses, are different in each approach. These results again suggest that the modification of the electron band structure caused by the two-dimensional geometric confinement plays an important role in determining the electron mobility.

V. CONCLUSIONS

We have investigated the electron mobility of Si nanowires with three crystalline orientations by considering the atomistic electron-phonon interactions. We have calculated the electron band structures based on the semiempirical $sp^3d^5s^*$ TB approach and the phonon band structures based on the Keating potential model. By combining the electron and phonon eigenstates based on Fermi's golden rule and solving the Boltzmann transport equation, we have evaluated the electron mobility of Si nanowires. As a result, the electron and phonon eigenstates in Si nanowires were found to be significantly dependent on the crystalline orientation and diameter. As expected, nanowire confinement modifies the atomic vibration mode and sound velocity, and therefore phonons in Si nanowires behave quite differently from those in bulk Si. However, the electron mobility of Si nanowires was found to be primarily governed by the variation in the electron effective mass rather than that in the phonon eigenstates. Accordingly, the $\langle 110 \rangle$-oriented Si nanowires showed the highest electron mobility, because they have the smallest electron effective mass among the three orientations. The results here also suggest that the isotropic deformation potential using the bulk natures of phonons still works for projection of a qualitative trend in electron transport in Si nanowires.

ACKNOWLEDGMENTS

This work was supported by a Grant-in-Aid for Scientific Research from the Japan Society for the Promotion of Science (JSPS), and the Japan Science and Technology Agency (JST/CREST).

APPENDIX A: ATOMISTIC POISSON EQUATION

The three-dimensional Poisson equation is solved using an atomistic mesh to define the electrostatic potential at all atomic positions in the unit cell, and the resulting electrostatic potential is substituted into the diagonal on-site matrix element of the TB Hamiltonian in Eq. (3). In this Appendix, we describe a finite volume discretization scheme adopted to solve the atomistic Poisson equation.

First, a three-dimensional Voronoi tessellation is provided for a given set of atomic positions in the Si nanowire, and then the Voronoi polyhedron is decomposed into tetrahedra with 4 triangular pyramids attached at every 4 equilateral triangles. Therefore, the Voronoi polyhedron has 16 faces with 4 regular hexagons and 12 triangles. Here, we define the atomic distance between the first (second) nearest-neighbor atoms as d_1 (d_2), and d_1 and d_2 are represented using the Si lattice constant a as shown,

$$d_1 = \frac{\sqrt{3}}{4}a, \quad d_2 = \frac{1}{\sqrt{2}}a. \tag{A1}$$

Next, the Voronoi surface between the first (second) nearest-neighbor atoms S_1 (S_2) and the Voronoi volume Δ are given by

$$S_1 = \sqrt{3}(d_1)^2, S_2 = \frac{\sqrt{2}}{12}(d_1)^2, \quad \Delta = \frac{8}{9}\sqrt{3}(d_1)^3. \tag{A2}$$

By using these variables, the atomistic three-dimensional Poisson equation is expressed in the finite volume method using the following equation:

$$\sum_{\eta',\kappa' \in 1NN(\eta,\kappa)} \frac{\varepsilon_{\eta\kappa,\eta'\kappa'}}{d_1} S_1(\phi_{\kappa'} - \phi_\kappa) + \sum_{\eta',\kappa' \in 2NN(\eta,\kappa)} \frac{\varepsilon_{\eta\kappa,\eta'\kappa'}}{d_2} S_2(\phi_{\kappa'} - \phi_\kappa) = en_\kappa. \tag{A3}$$

Here, $\varepsilon_{\eta\kappa,\eta'\kappa'}$ is the permittivity, and $1NN(\eta,\kappa)$ and $2NN(\eta,\kappa)$ represent the first and second nearest-neighbor atoms, respectively. Also, the atomic charge at the (η,κ) th atom in the right-hand side of Eq. (3) is calculated by

$$n_\kappa = \frac{4L}{2\pi}\sum_n \sum_\gamma \int_0^{\pi/L} dk |c^n_{\kappa,\gamma}(k)|^2 f_0\left(E_n(k)\right). \tag{A4}$$

The gate dielectric was considered by giving the permittivity of SiO_2 on the atomistic meshes in the region surrounding the nanowire, and the gate voltage was provided using the Dirichlet boundary condition at the gate/SiO_2 interfaces.

APPENDIX B: ANALYTICAL EXPRESSIONS OF ELECTRON-PHONON INTERACTION HAMILTONIAN MATRICES

In this study, we assumed the onsite energy to be unchanged by atomic vibration, and hence we describe here the theoretical derivations of the analytical spatial derivatives of the coupling matrices between the *s*-, *p*-, and *d*-orbitals.

By using the fact that the first spatial derivatives of the TB Hamiltonian matrix elements are expressed as a function of the directional cosines and the two-center integrals, their analytical expressions can be derived using the Slater-Koster parameters. First, we define the relative position vector from the nearest-neighboring *i*th to *j*th atoms $\mathbf{R}_{ij}$ by using its magnitude R_{ij} and unit vectors $\mathbf{e}_x$, $\mathbf{e}_y$, and $\mathbf{e}_z$ as follows:

$$\mathbf{R}_{ij} = \mathbf{R}_j - \mathbf{R}_i = R_{ij}(l_{ij}\mathbf{e}_x + m_{ij}\mathbf{e}_y + n_{ij}\mathbf{e}_z), \tag{B1}$$

where l_{ij}, mij, and n_{ij} are integers, and $R_{ij} = \sqrt{(x_j - x_i)^2 + (y_j - y_i)^2 + (z_j - z_i)^2}$ gives the distance between the nearest-neighbor atoms. As mentioned above, we need spatial derivatives of the matrix elements, so we introduce the following relationship between the first derivative of the bond length with respect to $\mathbf{R}_{ij}$ and the directional cosines (l_{ij}, m_{ij}, n_{ij}),

$$\frac{\partial R_{ij}}{\partial \mathbf{R}_{ij}} = \begin{bmatrix} l_{ij} \\ m_{ij} \\ n_{ij} \end{bmatrix}. \tag{B2}$$

Then, the spatial derivative of the two-center integrals is expressed as follows:

$$\frac{\partial V^{\zeta}_{i,j}(R_{ij})}{\partial \mathbf{R}_{ij}} = -\frac{n_\zeta V^{\zeta}_{i,j}(R^0_{ij})}{R_{ij}} \left(\frac{R^0_{ij}}{R_{ij}}\right)^{n_\zeta} \begin{bmatrix} l_{ij} \\ m_{ij} \\ n_{ij} \end{bmatrix}. \tag{B3}$$

Here, n_ζ is a generalized Harrison scaling parameter of the ζ bond, which was taken from Ref. 16 in the calculations.

Also, the first derivative of the directional cosines with respect to $\mathbf{R}_{ij}$ is expressed by

$$\frac{\partial}{\partial \mathbf{R}_{ij}} \begin{bmatrix} l_{ij} & m_{ij} & n_{ij} \end{bmatrix} = \frac{1}{R_{ij}} \begin{bmatrix} 1 - l_{ij}^2 & -l_{ij}m_{ij} & -l_{ij}n_{ij} \\ -m_{ij}l_{ij} & 1 - m_{ij}^2 & -m_{ij}n_{ij} \\ -n_{ij}l_{ij} & -n_{ij}m_{ij} & 1 - n_{ij}^2 \end{bmatrix}. \tag{B4}$$

In this study, the first derivatives of the Slater-Koster parameters are calculated using Eqs. (B3) and (B4). As an example, for the *s*-orbital and *p*-orbital coupling matrices, the following expressions were obtained:

$$\begin{aligned} \partial_{\mathbf{R}_{ij}} U^{s,s}_{i,j} &= \partial_{\mathbf{R}_{ij}} V^{ss\sigma}_{i,j}(R_{ij}), \\ \partial_{\mathbf{R}_{ij}} U^{s,p_x}_{i,j} &= (\partial_{\mathbf{R}_{ij}} l_{ij}) V^{sp\sigma}_{i,j}(R_{ij}) + l_{ij}\partial_{\mathbf{R}_{ij}} V^{sp\sigma}_{i,j}(R_{ij}), \\ \partial_{\mathbf{R}_{ij}} U^{s,p_y}_{i,j} &= (\partial_{\mathbf{R}_{ij}} m_{ij}) V^{sp\sigma}_{i,j}(R_{ij}) + m_{ij}\partial_{\mathbf{R}_{ij}} V^{sp\sigma}_{i,j}(R_{ij}), \\ \partial_{\mathbf{R}_{ij}} U^{s,p_y}_{i,j} &= (\partial_{\mathbf{R}_{ij}} n_{ij}) V^{sp\sigma}_{i,j}(R_{ij}) + n_{ij}\partial_{\mathbf{R}_{ij}} V^{sp\sigma}_{i,j}(R_{ij}), \end{aligned} \tag{B5}$$

The first spatial derivatives for all of the other matrix elements can be derived in the same manner. In fact, we derived one hundred expressions for first spatial derivatives of the nearest-neighbor coupling matrices to calculate the electron-phonon interaction Hamiltonian in Sec. III.

[1] N. Singh, A. Agarwal, L. K. Bera, T. Y. Liow, R. Yang, S. C. Rustagi, C. H. Tung, R. Kumar, G. Q. Lo, N. Balasubramanian, and D.-L. Kwong, IEEE Electron Device Lett. **27**, 383 (2006).
[2] C. Jungemann, A. Emunds, and W. Engl, Solid-State Electron. **36**, 1529 (1993).
[3] R. Kotlyar, B. Obradovic, P. Matagne, M. Stettler, and M. Giles, Appl. Phys. Lett. **84**, 5270 (2004).
[4] E. Ramayya, D. Vasileska, S. Goodnick, and I. Knezevic, J. Appl. Phys. **104**, 063711 (2008).
[5] S. Jin, M. V. Fischetti, and T.-W. Tang, J. Appl. Phys. **102**, 083715 (2009).
[6] C. Jacoboni and L. Reggiani, Rev. Mod. Phys. **55**, 645 (1983).
[7] A. Buin, A. Verma, and M. P. Anantram, J. Appl. Phys. **104**, 053716 (2008).
[8] F. Murphy-Armando, G. Fagas, and J. Greer, Nano Lett. **10**, 869 (2010).
[9] N. Neophytou and H. Kosina, Phys. Rev. B **84**, 085313 (2011).
[10] W. Zhang, C. Delerue, Y. M. Niquet, G. Allan, and E. Wang, Phys. Rev. B **82**, 115319 (2010).
[11] J. Slater and G. Koster, Phys. Rev. **94**, 1498 (1954).
[12] J. M. Jancu, R. Scholz, F. Beltram, and F. Bassani, Phys. Rev. B **57**, 6493 (1998).
[13] P. N. Keating, Phys. Rev. **145**, 637 (1966).
[14] S. Lee, F. Oyafuso, P. v. Allmen, and G. Klimeck, Phys. Rev. B **69**, 045316 (2004).
[15] T. B. Boykin, G. Klimeck, and F. Oyafuso, Phys. Rev. B **69**, 115201 (2004).
[16] T. B. Boykin, N. Kharche, and G. Klimeck, Phys. Rev. B **76**, 035310 (2007).
[17] D. R. Fokkema, G. L. G. Sleijpen, and H. A. Van der Vorst, SIAM J. Sci. Comput. **20**, 94 (1998).
[18] Y. Saad, *Iterative Methods For Sparse Linear Systems*, 2nd ed. (Society for Industrial Mathematics, Philadelphia, 2003).
[19] N. Neophytou, A. Paul, M. S. Lundstrom, and G. Klimeck, IEEE Trans. Electron Devices **55**, 1286 (2008).
[20] T. Maegawa, T. Yamauchi, T. Hara, H. Tsuchiya, and M. Ogawa, IEEE Trans. Electron Devices **56**, 553 (2009).
[21] M. Bescond, N. Cavassilas, and M. Lannoo, Nanotechnology **18**, 255201 (2007).
[22] E. Anderson, Z. Bai, C. Bischof, S. Blackford, J. Demmel, J. Dongarra, J. Du Croz, A. Greenbaum, S. Hammarling, A. McKenney, and D. Sorensen, *LAPACK User's Guide* (SIAM, Philadelphia, 1999).
[23] T. Thonhauser and G. D. Mahan, Phys. Rev. B **69**, 075213 (2004).
[24] C. Kittel, *Introduction to Solid State Physics*, 7th ed. (John Wiley & Sons, New York, 1996).
[25] M. Luisier and G. Klimeck, Phys. Rev. B **80**, 115430 (2009).
[26] D. Esseni, P. Palestri, and L. Selmi, *Nanoscale MOS Transistors: Semi-Classical Transport and Applications* (Cambridge University Press, Cambridge, 2011).
[27] J. M. Ziman, *Electrons and Phonons: The Theory of Transport Phenomena in Solids* (Oxford University Press, USA, 2001).
[28] G. Mahan, *Many-Particle Physics*, 2nd ed. (Plenum, New York, 1990).
[29] O. D. Restrepo, K. Varga, and S. T. Pantelides, Appl. Phys. Lett. **94**, 212103 (2009).
[30] K. Uchida, T. Krishnamohan, K. C. Saraswat, and Y. Nishi, *Tech. Dig. -Int. Electron Devices Meet.* 135 (2005).